Cyclic deformation leads to defect healing and strengthening of small-volume metal crystals

Zhang-Jie Wang[a], Qing-Jie Li[b], Yi-Nan Cui[c], Zhan-Li Liu[c], Evan Ma[a,b], Ju Li[a,d,e], Jun Sun[a], Zhuo Zhuang[c], Ming Dao[e,1], Zhi-Wei Shan[a,1], and Subra Suresh[f,1]

[a]Center for Advancing Materials Performance from the Nanoscale and Hysitron Applied Research Center in China, State Key Laboratory for Mechanical Behavior of Materials, Xi'an Jiaotong University, Xi'an 710049, China; [b]Department of Materials Science and Engineering, Johns Hopkins University, Baltimore, MD 21218; [c]Applied Mechanics Laboratory, School of Aerospace, Tsinghua University, Beijing 100084, China; [d]Department of Nuclear Science and Engineering, Massachusetts Institute of Technology, Cambridge, MA 02139; [e]Department of Materials Science and Engineering, Massachusetts Institute of Technology, Cambridge, MA 02139; and [f]Department of Materials Science and Engineering, Carnegie Mellon University, Pittsburgh, PA 15213

Contributed by Subra Suresh, September 15, 2015 (sent for review August 15, 2015)

When microscopic and macroscopic specimens of metals are subjected to cyclic loading, the creation, interaction, and accumulation of defects lead to damage, cracking, and failure. Here we demonstrate that when aluminum single crystals of submicrometer dimensions are subjected to low-amplitude cyclic deformation at room temperature, the density of preexisting dislocation lines and loops can be dramatically reduced with virtually no change of the overall sample geometry and essentially no permanent plastic strain. This "cyclic healing" of the metal crystal leads to significant strengthening through dramatic reductions in dislocation density, in distinct contrast to conventional cyclic strain hardening mechanisms arising from increases in dislocation density and interactions among defects in microcrystalline and macrocrystalline metals and alloys. Our real-time, in situ transmission electron microscopy observations of tensile tests reveal that pinned dislocation lines undergo shakedown during cyclic straining, with the extent of dislocation unpinning dependent on the amplitude, sequence, and number of strain cycles. Those unpinned mobile dislocations moving close enough to the free surface of the thin specimens as a result of such repeated straining are then further attracted to the surface by image forces that facilitate their egress from the crystal. These results point to a versatile pathway for controlled mechanical annealing and defect engineering in submicrometer-sized metal crystals, thereby obviating the need for thermal annealing or significant plastic deformation that could cause change in shape and/or dimensions of the specimen.

fatigue | dislocation motion | pristine materials | yield strength | cyclic mechanical healing

Metal single crystals of submicrometer dimensions with very low initial defect density often exhibit ultrahigh strength (1, 2) and large elastic strain, which offer opportunities for obtaining unprecedented physical and chemical characteristics by elastic strain engineering (3). High-temperature crystal growth (4, 5) or thermal annealing to eliminate structural defects such as dislocations (6) serves as a traditional route to produce such nearly pristine materials that are essentially free of defects.

Research in recent years has shown that monotonic loading can reduce or even eliminate dislocations in submicroscale single crystals (1, 7, 8). Such "mechanical annealing," however, comes at the expense of severe plastic deformation and significant changes in shape and/or dimensions of the crystal (9–12). Mechanical annealing could potentially serve as an attractive pathway for tailoring the properties of nanoscale devices in such applications as nanoprint embossing (13, 14) and electronics (15, 16), if defects could be eliminated by recourse to nondestructive means that do not introduce changes in crystal shape and/or dimensions.

A dislocation in the vicinity of a free surface experiences an image force that tends to draw the defect toward the surface, with the magnitude of the force increasing as the dislocation moves closer to the free surface with an attendant reduction in its stored elastic energy (17). Here we hypothesize that one possible route to achieve mechanical healing in a metal single crystal would, therefore, entail the application of an external stress that is large enough to induce preexisting dislocations to move from their initial positions so that the image forces from the free surfaces of the small crystal could then attract them to the surface to facilitate their egress from the crystal. At the same time, we also envision that the externally imposed stress should not be large enough to introduce new dislocations either by heterogeneous surface nucleation or by dislocation interactions. The challenge in addressing these competing effects stems from the fact that the configuration of the preexisting dislocations could be extremely complex and that the critical stress necessary to activate or annihilate them may be high enough to generate new dislocations. Inspired by the common observation that it is much easier to pull out a partly buried object by shaking it first, we hypothesize that imposition of low amplitudes of cyclic straining could serve as an effective means to disengage those complex preexisting dislocation configurations in a crystal. Such fatigue-induced mechanical annealing would entail repeated low-stress amplitude loading that would cause "healing" by inducing pinned dislocations to move by dislodging them to be drawn toward the nearest free surface; the stress amplitude should not be large enough to facilitate the nucleation of new dislocations at surface heterogeneities or to foster the onset and growth of fatigue cracks (18).

Significance

Producing strong and defect-free materials is an important objective in developing many new materials. Thermal treatments aimed at defect elimination often lead to undesirable levels of strength and other properties. Although monotonic loading can reduce or even eliminate dislocations in submicroscale single crystals, such "mechanical healing" causes severe plastic deformation and significant shape changes. Inspired by observing an easier pullout of a partly buried object after shaking it first, we demonstrate that "cyclic healing" of the small-volume single crystals can indeed be achieved through repeated low-amplitude straining. The cyclic healing method points to versatile avenues for tailoring the defect structure and strengthening of nanoscale metal crystals without the need for thermal annealing or severe plastic deformation.

Author contributions: Z.-J.W., Q.-J.L., E.M., J.L., J.S., Z.Z., M.D., Z.-W.S., and S.S. designed research; Z.-J.W., Q.-J.L., Y.-N.C., and Z.-L.L. performed research; Z.-J.W., Q.-J.L., Y.-N.C., Z.-L.L., E.M., J.L., J.S., Z.Z., M.D., Z.-W.S., and S.S. analyzed data; and Z.-J.W., Q.-J.L., E.M., J.L., M.D., Z.-W.S., and S.S. wrote the paper.

The authors declare no conflict of interest.

Freely available online through the PNAS open access option.

[1]To whom correspondence may be addressed. Email: mingdao@mit.edu, zwshan@mail.xjtu.edu.cn, or suresh@cmu.edu.

This article contains supporting information online at www.pnas.org/lookup/suppl/doi:10.1073/pnas.1518200112/-/DCSupplemental.

We demonstrate the validity of our hypothesis here by presenting unique experimental results of mechanical healing in pure aluminum single crystals, which are subjected to low-amplitude cyclic straining inside a transmission electron microscope (TEM). The experimental setup is shown in Fig. 1*A*, where the diamond grip used to impose a tensile strain on the dog-bone–shaped specimen is shown. Both the grip and the specimen were fabricated using the focused ion beam (FIB) technique. Two reference markers were purposely fabricated on the specimen to allow for accurate measurement of strain in the gauge section of an aluminum single crystal, 300 nm thick and 500 nm wide (Fig. 1 *A*–*C*). All of the tests were carried out at room temperature, under displacement rate control at a cyclic frequency of 0.45 cycle/s. The loading axis was along the $[\bar{1}11]$ crystallographic direction of the face-centered cubic (FCC) Al crystal, and the beam direction was close to the [110] zone axis, as confirmed by the selected area electron diffraction pattern. Two types of dislocations were identified in the as-fabricated aluminum crystal: dislocation lines inherited from the bulk crystal or generated during the fabrication process and Frank dislocation loops introduced by ion beam irradiation during FIB cutting, which usually occur in the regions close to the free surface (19). The initial densities of dislocation lines and dislocation loops in the as-fabricated crystal specimen were measured to be $\sim 2.0 \times 10^{13}$ m^{-2} and 4.6×10^{13} m^{-2}, respectively (Fig. 1*D*).

Six groups of cyclic loading, G1–G6, were imposed on the aluminum crystal, with images of the crystal before cyclic loading and after completion of the G6 loading sequence shown in Fig. 1 *B* and *C*, respectively. The maximum nominal tensile strain applied on the crystal in this test was 0.006 (Table 1). By comparing Fig. 1 *B* and *C*, it is seen that at the end of loading sequence G6, essentially all dislocations in the gauge length in between the two markers were driven out of the crystal. This observation was also confirmed by tilt examination in the TEM (details in *SI Text*, Table S1, and Fig. S1). After about 700 loading cycles with a maximum imposed nominal tensile strain of 0.006 ± 0.002, the total accumulated tensile plastic strain in the gauge length of the specimen was assessed to be only 0.002 ± 0.001. This demonstrates that low-amplitude cyclic deformation can indeed result in mechanical healing, consistent with our hypothesis. The last (G6) loading led to failure outside the gauge section (at the location marked by the red arrow in the bottom left corner of Fig. 1*C*), where abundant dislocation populations were preserved. Note that the larger cross-section area outside of the gauge section implies a lower nominal stress than within the gauge section. The fact that plastic yielding is observed at the lower-stress area outside the gauge section also supports the notion

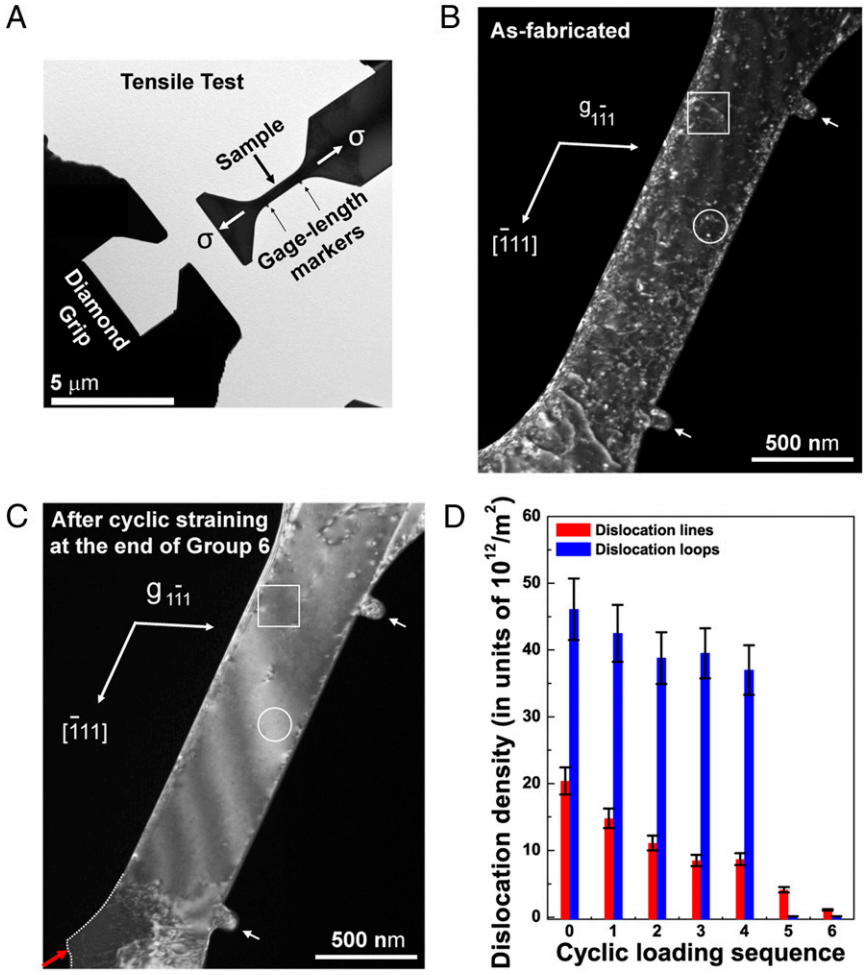

Fig. 1. Cyclic mechanical healing of the aluminum single crystal. (*A*) Experimental setup for quantitative real-time observations of cyclic tensile loading of the aluminum single crystal inside a TEM. (*B* and *C*) Dark-field TEM images of the single crystal before and after the cyclic mechanical healing treatment, respectively. *C* shows an essentially dislocation-free crystal at the scale of observation, whereas *B* shows preexisting dislocations. (*D*) Changes in the density of dislocation lines and dislocation loops after each cyclic straining sequence.

ENGINEERING

Table 1. Details of cyclic loading sequence for the Al crystal shown in Fig. 1

Cyclic loading sequence group no.	N	ε_{max}	ε_{min}	σ_{max}, MPa	σ_{min}, MPa	$\rho_{type\ I}$, 10^{12} m^{-2}	$\rho_{type\ II}$, 10^{12} m^{-2}	Image
As fabricated	0					20.4	46.1	Fig. 1*B*
G1	80	—	—	38	12	14.8	42.5	
G2	175	—	—	44	−23	11.1	38.8	
G3	80	—	—	170	16	8.5	39.5	
G4	65	—	—	90	0	8.7	37.0	
G5	300	0.004 ± 0.002	—	250	−92	4.1	0.13	
G6	1	0.006 ± 0.002	—	420	14	1.1	0.13	Fig. 1*C*

Note that the maximum strain values for G1–G4 and the minimum strain values for all six loading sequences were too small to be measured. They are indicated here as "—".

that the gauge length of the crystal has developed a higher strength due to mechanical healing through defect removal.

Dislocation lines in the crystal behaved differently from dislocation loops under repeated cyclic straining, as shown in Fig. 1*D* where the dislocation density is plotted as a function of loading sequence through the six groups of low-amplitude fatigue. The density of dislocation lines (shown by red bars in Fig. 1*D*) decreased gradually with cyclic straining. Here, change from one loading sequence to another, from G1 to G6, resulted in transient effects that were "shaken down" to a lower density state at the conclusion of each loading group except G4. The extent of dislocation density drop in response to each loading group is determined by the peak stress differential with respect to the previous loading group. For example, if the nominal maximum tensile stress at the beginning of a loading sequence in a group was higher than that at the previous group (e.g., G1 to G2, G2 to G3, G4 to G5, and G5 to G6), extensive dislocation escape occurred at the free surface that gradually stabilized to a lower dislocation density by the time the end of the loading sequence in that group was reached. However, if the maximum stress level was lowered compared with that in the previous loading group (e.g., G3 to G4), little change could be detected in the density of dislocation lines. Specifically, when the stress was lowered from 170 MPa (loading sequence G3) to 90 MPa (loading sequence G4), the density of dislocation lines remain unchanged (Table 1). This indicates that the critical stress for dislocation lines to be activated occurs over a stress range of tens of megapascals to a few hundred megapascals. By contrast, for the first four loading sequences, G1–G4, the density of dislocation loops (Fig. 1*D*, blue bars) decreased only slightly. However, when the nominal stress was increased to 250 MPa, from G4 to G5, the density of dislocation loops dropped dramatically. This suggests that the nominal value of critical stress necessary to annihilate the dislocation loops is between 170 MPa and 250 MPa for the particular geometrical conditions of the experiment.

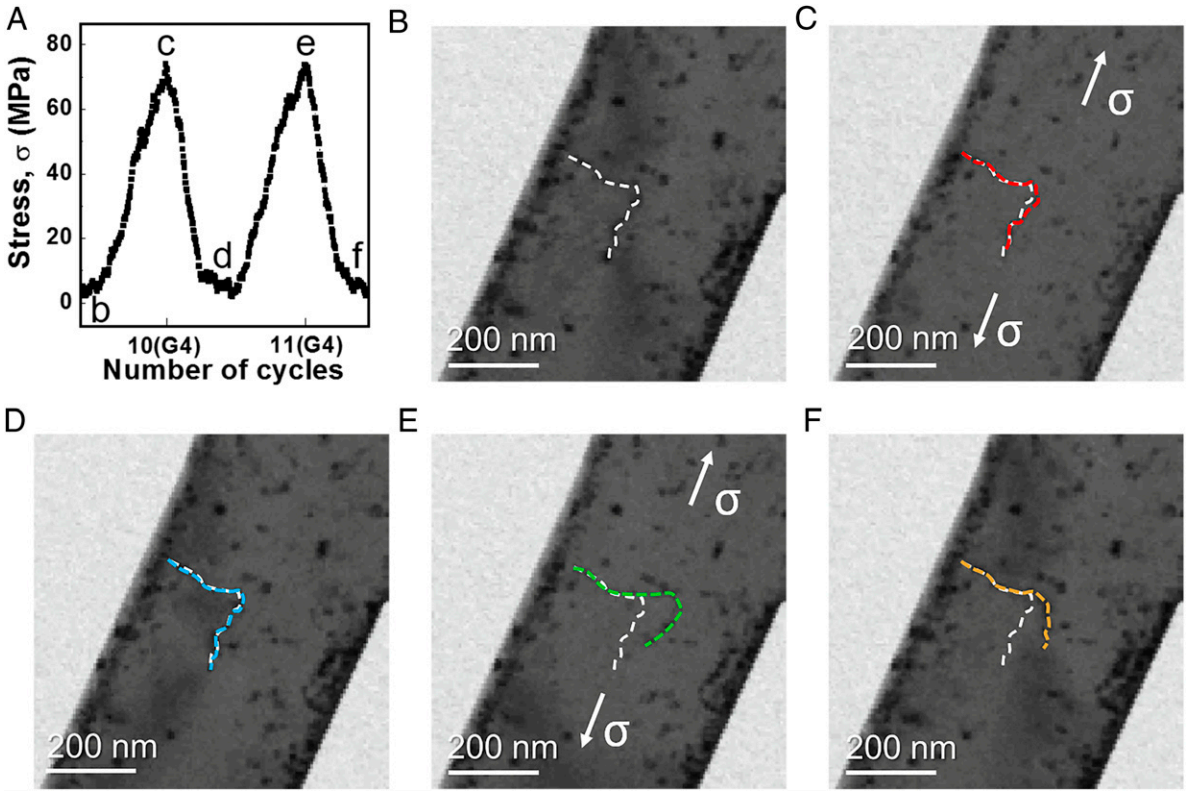

Fig. 2. Abrupt depinning and destabilization of a dislocation line due to repeated cyclic loading. (*A*) Evolution of nominal tensile stress during two selected cycles: 10 and 11 in loading sequence G4, described in Table 1. (*B*–*F*) Still frames extracted from Movie S1 that corresponds to the stress state marked in *A*. The direction of tensile straining is indicated by the arrows in *C* and *E*. (Scale bars in *B*–*F*, 200 nm.)

Detailed analysis of real-time, in situ video images from the TEM experiments revealed that in response to cyclic loading, pinned dislocation lines first experienced oligodynamic motion over many cycles before exhibiting a sudden and dramatic change in morphology. One typical example is shown in Fig. 2. The highlighted dislocation line in Fig. 2 is the same one framed by the white rectangle in Fig. 1*B*. The nominal engineering stress of cycles 10 and 11 in loading sequence G4 is shown in Fig. 2*A*. The still frames extracted from Movie S1 corresponding to the stress states marked *b*–*f* in Fig. 2*A* are shown in Fig. 2 *B*–*F*, respectively. The profile of the curved dislocation chosen in this illustrative example is delineated in turn with white (Fig. 2*B*), red (Fig. 2*C*), light blue (Fig. 2*D*), green (Fig. 2*E*), and brown (Fig. 2*F*) dashed lines, with a different color chosen to represent the (changing) dislocation positions corresponding to those points marked in Fig. 2*A*. At the end of loading cycle 10, denoted as position *d* (Fig. 2*A*), the profile of the curved dislocation was only slightly different from that at the start of this loading cycle, denoted as *b* (Fig. 2*D*). A similar scenario was observed during the loading cycles before cycle 10 in loading sequence G4. However, the dislocation broke away from its original pinned position during loading cycle 11 (Fig. 2*E*) and changed its profile significantly from *d* to *f* (compare Fig. 2 *D* and *F*). Our observations from video images reveal that dislocation loops frequently served as pinning points for dislocation lines. Incremental changes in dislocation position and morphology in response to cyclic straining were often followed by an abrupt change; this pattern repeated until the dislocation was driven out of the crystal.

In the first set of experiments described thus far, protruding markers were introduced in the single crystal, as noted earlier, to delineate clearly the gauge length of the specimen within which dislocation density and cyclic strain could be quantitatively determined. Although the presence of these markers provided reproducible trends in the overall mechanistic response, these protrusions could also serve as local stress concentrators that influence local dislocation density evolution (Movie S2). To avoid this artifact and to demonstrate further that mechanical healing occurs without the presence of these markers, aluminum single-crystal specimens without markers were fabricated using FIB processing.

In all, we tested three specimens without protruding markers and six specimens with protruding markers. Fig. 1 provides a typical example of results obtained for specimens with protruding markers. All of the tests reported in this work were carried out under displacement rate control. To avoid introducing additional plastic deformation and transient cyclic deformation behavior, we purposely started to load all of the samples gradually from small displacement amplitudes. The normal stress was calculated to be the engineering stress, which is the readout force divided by the cross-sectional area.

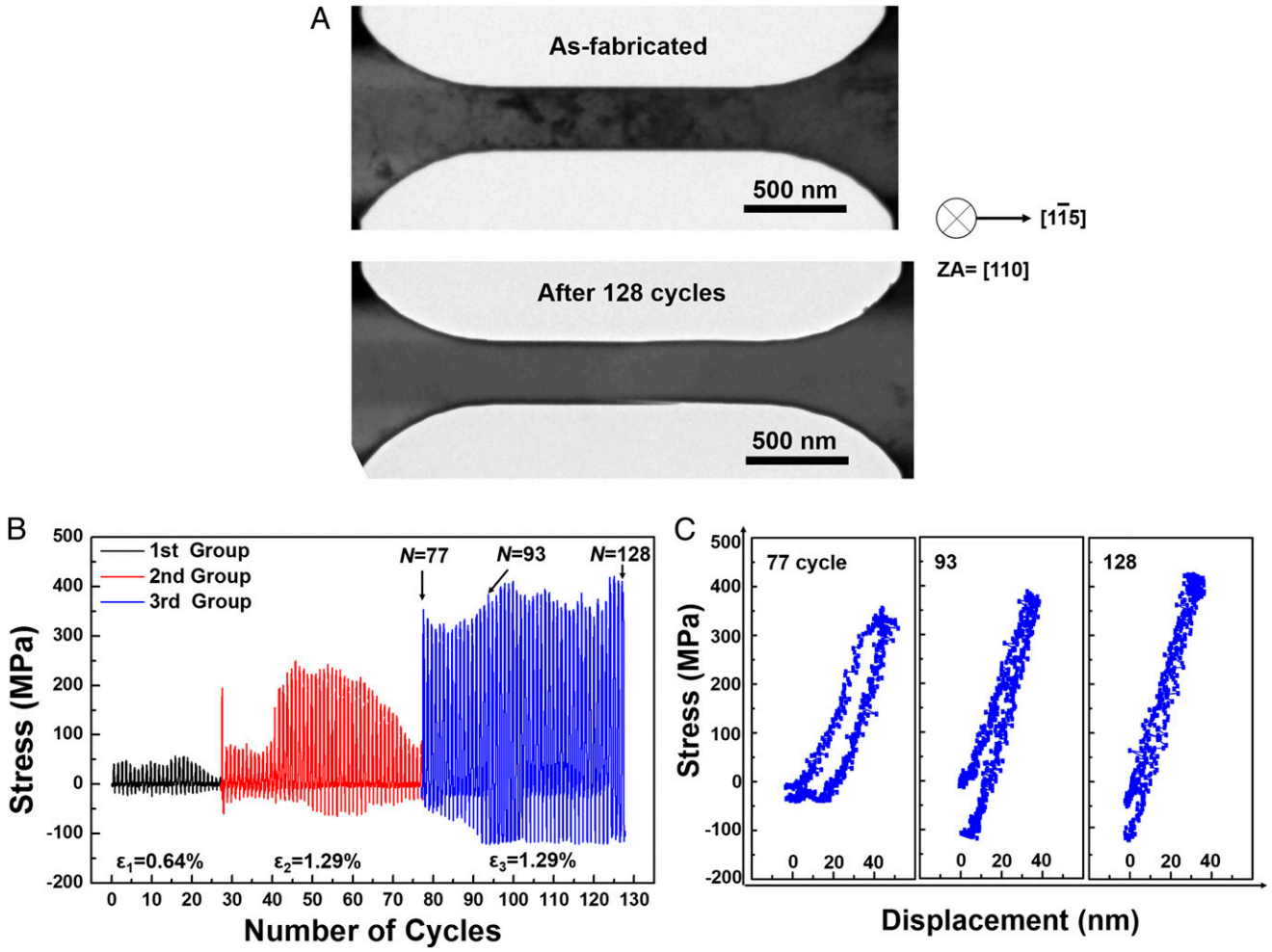

Fig. 3. Changes in deformation characteristics of Al single crystal from mechanical healing. (*A*) Bright-field images of aluminum single crystal before (*Top*) and after (*Bottom*) mechanical healing. (*B*) Detailed loading parameters and the stress vs. number of cycles. (*C*) The force vs. displacement curves during different loading cycles, $n = 77$, $n = 93$, and $n = 128$.

One typical example from a specimen without the protruding reference markers is shown in Fig. 3, where the specimen was 350 nm in thickness and 387 nm wide. The loading axis was along the [1$\bar{1}$5] direction and the beam direction was close to the [110] zone axis. Preexisting dislocations could be seen in the as-fabricated sample (Fig. 3*A*, *Top*). Three groups of cyclic straining were carried out to eliminate defects in the specimen. The corresponding stress vs. number of cycles is plotted in Fig. 3*B*. The nominal strain amplitudes used in these three groups of cyclic loadings were 0.64% (black), 1.29% (red) and 1.29% (blue), respectively. The abnormal stress evolution observed in the second group of cyclic loading (between cycles 28 and 40) was due to the uneven plastic deformation and a transient bending load resulted from unsymmetrically escaped dislocations. After repositioning the grip to compensate for the small tensile plastic strain generated during the second group of cyclic straining (Fig. S2), the third group of cyclic straining yielded an apparently pristine crystal. As shown in Fig. 3*A*, *Bottom*, no dislocations could be detected in the gauge section after 128 loading cycles. The specimen width was altered by less than 0.52% during cyclic loading that resulted in mechanical healing. Fig. 3*C* shows a plot of the nominal tensile stress as a function of the nominal tensile displacement of the specimen in 77, 93, and 128 cycles. Note that the area of the hysteresis loop exhibited by the stress–displacement curve diminishes with increasing number of cycles, as the crystal is mechanically healed through low-amplitude fatigue loading by eliminating dislocations. For this set of experiments, the dislocation density in the gauge section of the as-fabricated specimen was measured to be 5.47×10^{13} m^{-2}. After 77 cycles, this dislocation density decreased to 6.49×10^{12} m^{-2}. For $n = 93$ and $n = 128$, the density of visible dislocations dropped to essentially zero. When the gauge section of the crystal visibly becomes free of dislocations after 128 cycles, the associated stress–displacement also becomes free of hysteresis, thereby indicating a nearly fully reversible elastic deformation response during cyclic loading. The negative nominal stress upon unloading (Fig. 3 *B* and *C*) and the small mismatch between the loading and unloading segments of the curve are a consequence of adhesion between the grip and the specimen as well as plastic deformation outside of the gauge section (*SI Text* and Fig. S2). Subsequent monotonic loading in the strain-to-failure test demonstrated that this specimen yielded at a stress as high as 800 MPa followed by an abrupt stress drop and a large strain burst (red curve in Fig. 4).

Three key parameters dominate the healing effect: stress amplitude, number of cycles, and the loading sequence. Fig. 4 is a plot of the nominal maximum tensile stress as a function of nominal plastic strain during the strain-to-failure test of four specimens that were subjected to different mechanical fatigue healing treatments. The red curve in Fig. 4 (specimen S1) shows the data points for the specimen without protruding markers, for which results are presented in Fig. 3. The other three sets of data in Fig. 4 are from specimens that contained protruding markers. Specimen S2 was cycled 150 times under 200 MPa and 150 times under 550 MPa. Specimen S3 was cycled 50 times under 200 MPa and 50 times under 425 MPa. Specimen S4 is the as-fabricated specimen without any cyclic loading treatment. These results indicate that the mechanical properties of submicron-sized samples could be tailored through cyclic mechanical healing by the appropriate selection of stress amplitude, number of cycles, and the loading sequence.

These results conclusively show that mechanical healing by defect elimination can be achieved by recourse to low-amplitude cyclic deformation, which leads to significantly improved apparent yield strength. The method demonstrated here thus offers a unique means to tune mechanical properties of submicron-sized metal crystals through cyclic loading while at the same time preserving its overall geometry. Microscale and macroscale FCC metal crystals subjected to low-amplitude cyclic loading generally

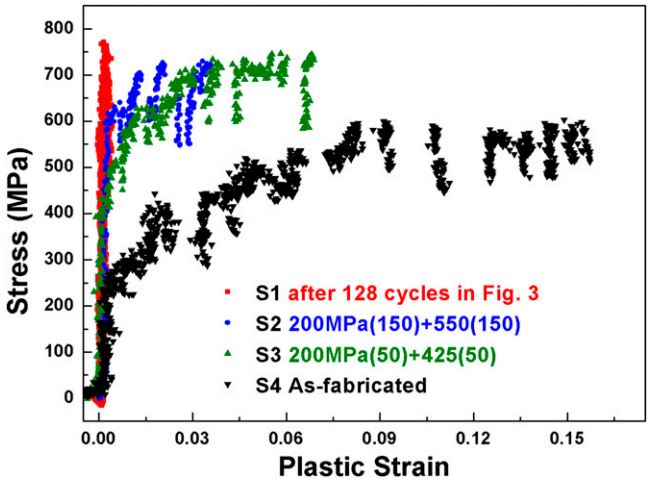

Fig. 4. Engineering stress plotted as a function of plastic strain from strain-to-failure experiments on four specimens with different degrees of cyclic mechanical healing. The cyclic loading parameters are described in terms of maximum tensile stress (in megapascals) and number of cycles within each loading sequence (cited in parentheses).

exhibit easier nucleation and growth of fatigue cracks concomitantly with the development of unique dislocation patterns (such as edge dislocation dipoles forming vein-like structures as well as ladder-like structures known as persistent slip bands) than monotonic loading of the same maximum nominal tensile stress (18). The continual increases in dislocation density during cyclic loading, concomitantly with interactions among dislocations that produce geometric patterns that are unique to fatigue deformation, are known to be precursors for surface features such as intrusions and extrusions. These surface features are known to be sites at which fatigue cracks are formed in single-crystalline and polycrystalline metals and alloys of microscopic and macroscopic dimensions. These mechanisms of dislocation generation and rearrangement in conventional fatigue processes also influence cyclic strain hardening or cyclic strain softening in metals and alloys (18). However, our results presented here show that submicroscale pure Al crystals, when subjected to cyclic loading, exhibit strengthening through elimination of preexisting dislocations under appropriate conditions, without developing fatigue cracks.

Our experiments also indicate that even specimens that undergo full mechanical healing exhibit posthealing yield strength well below the theoretical strength. For example, the yield strength of the crystal in Fig. 3 is only ~800 MPa after mechanical healing (red curve in Fig. 4), whereas its theoretical strength is on the order of several gigapascals. This can be rationalized by noting that, although dislocations are removed during cyclic loading, slip steps will be created on sample surfaces (20). Consequently, the specimen surfaces are still susceptible to dislocation nucleation compared with an atomically smooth surface.

To verify whether slip steps at surfaces, of atomic spacing dimensions, of the aluminum crystal can lead to significant flow strength reduction, we conducted atomistic simulations, using quasistatic athermal loading to model athermal yield strength and the free-end nudged elastic band (FENEB) method to assess the activation energy of dislocation nucleation as a function of applied stress level. See *SI Text* for details of the procedures used to perform atomistic simulations. The results of atomistic simulations of the mechanical behavior of pristine aluminum single crystals without any surface steps and those with 1*b* height (where *b* is the magnitude of the Burgers vector) surface steps are shown in Fig. S3. These results provide a mechanistic rationale

for the experimental observations that cyclically healed Al single crystals exhibit flow strengths that are well below the theoretical limit values.

In summary, the in situ experiments described here demonstrate that cyclic healing of the small-volume Al single crystals could be achieved through low-amplitude cyclic deformation. By performing these unique experiments inside a TEM, we have observed the forward and reverse movements of dislocations during the loading and unloading cycles. The irreversibility of such dislocation motion leads to the unpinning of a population of dislocations that are pulled to the free surfaces of the crystal by image forces, which induce the dislocations to exit the crystal. The attendant drastic reduction in dislocation density of the crystal causes cyclic healing, which, in turn, results in a marked increase in the strength of the crystal.

These results of cyclic-strain–induced healing and strengthening of the nanoscale, small-volume single crystals are in distinct contrast to traditional processes associated with cyclic strain hardening or softening of micrograined, large-volume metals and alloys of monocrystalline and polycrystalline structures (18). Consider, for example, the specific case of copper, where rapid increases in cyclic yield strength are commonly observed as a consequence of continuous generation and reorganization of dislocation structures during cyclic loading, which lead to unique geometric patterns such as dislocation vein structures, ladder structures composed of edge dislocation dipoles, and persistent slip bands (18). It is also known that specimens of copper with high initial dislocation density, such as those initially subjected to severe cold work, usually cyclically strain soften as the repeated cycling of the crystal leads to rearrangements of dislocations that seek a lower-energy equilibrium state (21, 22). Conversely, well-annealed copper specimens with low initial dislocation density cyclically strain harden as a result of fatigue-induced generation of dislocations whose interactions significantly strengthen the crystal and lead to an equilibrium state that remarkably has the same steady-state strength characteristics as the initially cold-worked copper subjected to cyclic loading (21, 22). Similar results were also reported in macroscopic specimens of polycrystalline copper, containing an initially low or high density of nanoscale twins, which were subjected to repeated frictional sliding (23). In this case, copper specimens with both a high and a low density of nanotwins eventually converged to a similar structure and local strength characteristic after repeated tribological deformation (23).

The results presented in this paper, by contrast, point to a different and unique mechanism of healing of a submicroscale metal crystal in response to cyclic deformation, whereby defect elimination and strengthening are achieved. Our work thus demonstrates unique avenues for tailoring the defect structure and strengthening of nanoscale metal crystals, thereby circumventing the need for thermal treatments or large plastic deformation that could lead to significant dimensional and shape changes.

Methods

Sample Preparation. The starting Al single crystal (>99.999% purity) had a thickness of 200 μm and diameter of 3 mm with a <110> normal direction. It was polished mechanically on both sides to a thickness of 50 μm. One side was then subjected to twin-jet polishing in a chemical solution of methanol with 5% (vol/vol) perchloric acid to obtain a thin region with a thickness of several micrometers. Next, this sample was glued to a specially designed copper support with its thin region facing out. Inside the thin region, thin plates with dimensions of 500 nm (thickness) × 3 μm (width) × 5 μm (length) were fabricated by using a FIB. The long edge of this thin plate was carefully aligned to be parallel to the loading axis. During this step, the beam current was gradually decreased from 21 nA to 93 pA while the accelerating voltage of the ion beam was kept at 30 KeV. Then T-shaped samples were FIBed into the thin plate through a flexible-designed bitmap pattern and the beam current used for this step was 28 pA. The middle region was thinned to electron transparent with a beam current of 1.5 pA.

In Situ Tensile Test. The in situ tensile experiments were carried out inside a JEM 2100 field emission gun TEM (JEOL), using a PicoIndenter (PI95) (Hysitron) under displacement control mode. The corresponding microstructure evolution was recorded using a Gatan 833 CCD camera (SC200).

ACKNOWLEDGMENTS. This work was supported by the Natural Science Foundation of China (51231005, 11132006, 51401159, and 51321003), the 973 Programs of China (2012CB619402), and the 111 project (B06025). J.L. acknowledges support by National Science Foundation Grants DMR-1120901 and DMR-1410636. Q.-J.L. and E.M. acknowledge support from the US Department of Energy, Basic Energy Science, Division of Materials Sciences and Engineering, under Contract DE-FG02-09ER46056. M.D. acknowledges support from the Singapore–Massachusetts Institute of Technology Alliance.

1. Shan ZW, Mishra RK, Syed Asif SA, Warren OL, Minor AM (2008) Mechanical annealing and source-limited deformation in submicrometre-diameter Ni crystals. *Nat Mater* 7(2):115–119.
2. Kiener D, Minor AM (2011) Source truncation and exhaustion: Insights from quantitative in situ TEM tensile testing. *Nano Lett* 11(9):3816–3820.
3. Li J, Shan ZW, Ma E (2014) Elastic strain engineering for unprecedented materials properties. *MRS Bull* 39(2):108–117.
4. Brenner SS (1958) Growth and properties of "whiskers": Further research is needed to show why crystal filaments are many times as strong as large crystals. *Science* 128(3324):569–575.
5. Richter G, et al. (2009) Ultrahigh strength single crystalline nanowhiskers grown by physical vapor deposition. *Nano Lett* 9(8):3048–3052.
6. Lowry MB, et al. (2010) Achieving the ideal strength in annealed molybdenum nanopillars. *Acta Mater* 58(15):5160–5167.
7. Hemker KJ, Nix WD (2008) Nanoscale deformation: seeing is believing. *Nat Mater* 7(2): 97–98.
8. Huang L, et al. (2011) A new regime for mechanical annealing and strong sample-size strengthening in body centred cubic molybdenum. *Nat Commun* 2(11):547.
9. Wang Z-J, et al. (2012) Sample size effects on the large strain bursts in submicron aluminum pillars. *Appl Phys Lett* 100(7):071906.
10. Chisholm C, et al. (2012) Dislocation starvation and exhaustion hardening in Mo alloy nanofibers. *Acta Mater* 60(5):2258–2264.
11. Greer JR, Nix WD (2006) Nanoscale gold pillars strengthened through dislocation starvation. *Phys Rev B* 73(24):245410.
12. Wang Z-J, Shan Z-W, Li J, Sun J, Ma E (2012) Pristine-to-pristine regime of plastic deformation in submicron-sized single crystal gold particles. *Acta Mater* 60(3): 1368–1377.
13. Jiao LY, et al. (2005) Fabrication of metallic nanostructures by negative nanoimprint lithography. *Nanotechnology* 16(12):2779–2784.
14. Rowland HD, King WP, Pethica JB, Cross GLW (2008) Molecular confinement accelerates deformation of entangled polymers during squeeze flow. *Science* 322(5902): 720–724.
15. Nakamura S (1998) The roles of structural imperfections in InGaN-based blue light-emitting diodes and laser diodes. *Science* 281(5379):955–961.
16. Nakamura D, et al. (2004) Ultrahigh-quality silicon carbide single crystals. *Nature* 430(7003):1009–1012.
17. Hirth JP (1982) *Theory of Dislocations* (Wiley, New York), 2nd Ed.
18. Suresh S (1998) *Fatigue of Materials* (Cambridge Univ Press, Cambridge, UK), 2nd Ed.
19. Idrissi H, et al. (2011) Point defect clusters and dislocations in FIB irradiated nanocrystalline aluminum films: An electron tomography and aberration-corrected high-resolution ADF-STEM study. *Microsc Microanal* 17(6):983–990.
20. Zheng H, et al. (2010) Discrete plasticity in sub-10-nm-sized gold crystals. *Nat Commun* 1:144.
21. Feltner CE, Laird C (1967) Cyclic stress-strain response of FCC metals and alloys. 1. Phenomenological experiments. *Acta Metall* 15(10):1621–1632.
22. Feltner CE, Laird C (1967) Cyclic stress-strain response of F.C.C. metals and alloys. 2. Dislocation structures and mechanisms. *Acta Metall* 15(10):1633–1653.
23. Singh A, Dao M, Lu L, Suresh S (2011) Deformation, structural changes and damage evolution in nanotwinned copper under repeated frictional contact sliding. *Acta Mater* 59(19):7311–7324.
24. Plimpton S (1995) Fast parallel algorithms for short-range molecular dynamics. *J Comput Phys* 117(1):1–19.
25. Zope RR, Mishin Y (2003) Interatomic potentials for atomistic simulations of the Ti-Al system. *Phys Rev B* 68(2):024102.
26. Henkelman G, Jonsson H (1999) A dimer method for finding saddle points on high dimensional potential surfaces using only first derivatives. *J Chem Phys* 111(15): 7010–7022.

Supporting Information

Wang et al. 10.1073/pnas.1518200112

SI Text

Tilt Examination of Dislocations in the Transmission Electron Microscope. Table S1 summarizes the visibility of dislocations with various Burgers vectors when they are observed under dark-field imaging mode with different reflection vectors. To confirm the depletion of the dislocations in the gauge section, we purposely tilted the Al sample shown in Fig. 1 to [334] zone axis (ZA) and imaged it under $[2\bar{2}0]$ and $[31\bar{3}]$ reflection vectors. As shown in Fig. S1 *A* and *B*, few dislocations can be detected in the gauge part, which confirms that dislocation density was reduced dramatically in the gauge section of the specimen after mechanical healing.

The Origin of the Compressive Stress upon Unloading. The compressive (or negative) stress observed in our tests (e.g., Fig. 3 *B* and *C* in the main text) upon unloading can be attributed to a number of factors, as illustrated schematically in Fig. S2. The grip was programmed to travel within the region marked by the two red short lines, as shown in Fig. S2 *A* and *B*. At the very beginning, the minimum stress was zero. However, once the sample deformed plastically because of the escaped dislocations and/or the plastic fitting at the contact interface between the sample and the diamond grip, its length increased by ΔL. Because all of the tests were carried out under displacement-control mode, the grip was set to keep its programmed travel range. Consequently, the zero stress position was shifted by ΔL. Because of the adhesion force between the grip and the sample, a compressive stress would now be generated within the region framed by the right red line position and the new zero stress position (vertical dashed line), as shown in Fig. S2*B*.

Atomistic Simulations of the Mechanical Behavior of Pristine Aluminum Pillars Without and With a Surface Step. Fig. S3*A* shows the stress–strain curves from quasistatic athermal loading (QAL) simulations for a perfect Al pillar with an atomically smooth surface and for an Al pillar with a slip step of 1*b* height on a cylindrical surface by the escape of one dislocation along the {111} plane. Fig. S3*A*, *Inset* shows the orientation of the crystal for the loading simulation for these two cases. The results show that even a one-Burgers-vector height step can significantly reduce the athermal flow strength, by as much as 50%. Further calculations using the free-end nudged elastic band (FENEB) method evaluated the activation energy of dislocation nucleation as a function of applied stress level, as shown in Fig. S3*B*, which reveals that at the same applied stress, the activation energy for surface dislocation nucleation is decreased significantly (by an order of magnitude) for a pillar with stepped surfaces compared with that with an atomically smooth, perfect surface. The results in Fig. S3*B* imply further significant flow strength reduction, in addition to that shown in Fig. S3*A*, due to thermal energy activation.

For the atomistic computations, the large-scale molecular dynamics package, LAMMPS (24) was used to simulate the response of an Al single-crystal pillar of dimensions 23 × 11 × 11 nm. The axial orientation of the crystal was along [110] and the side surfaces were (001) and $(\bar{1}10)$. The empirical potentials (25) used here, describing the interaction between Al atoms, were developed using a large database of experimental and ab initio data. The basic physical properties (e.g., lattice constants, elastic constants, energy for vacancy formation and migration, stacking fault energy, equation of state to a large pressure range, etc.) generated by this potential were found to be in good agreement with experimental data. For QAL, the sample was first stretched by uniformly scaling the axial coordinate of each atom to a small strain and then kept at the current strain, and energy minimization was performed via the conjugate gradient method. This loading mode was repeated until the athermal stress level for surface dislocation nucleation was reached. The FENEB method is a useful reaction pathway sampling technique for stress-driven dislocation nucleation problems. Similar to the standard nudged elastic band (NEB) method, first a trial reaction pathway was generated by linearly interpolating the hyperspace coordinate (13) ($\{x_i\}$ is the lattice vector of atom i) of the system between an initial configuration and a final configuration. Usually, a finite number of intermediate images/replicas of the system were chosen from the trial reaction pathway, forming the so-called "band." These intermediate images/replicas generally are not exactly on the minimum energy pathway (MEP). Therefore, a constrained energy minimization procedure was performed to converge the band to the MEP while maintaining equal spacing between neighboring replicas. The constraint was applied by first adding an elastic force along the band such that each intermediate replica experienced a pulling/pushing force along the band, depending on their relative distances between the neighboring replicas. The initial state usually is not subjected to the elastic force (hence the term, "elastic band"). In addition to this elastic force constraint, atoms in each replica were subjected only to the potential energy force component perpendicular to the band. This forms the so-called "nudged elastic band." The overall effect is that the potential energy force component perpendicular to the band relaxes the replicas to the MEP while the elastic force along the band maintains an equal spacing between neighboring replicas. For the FENEB, a special treatment is applied to the final state; i.e., only elastic force along the band is considered. This means that the potential energy of the final state will remain constant and it is free to move on an isosurface of the potential energy landscape where the same potential energy is found. This is quite useful if the final state is not in a stable/metastable state. The reason is that it allows us to choose only a segment around the saddle point instead of using the whole band to perform the calculation. For dislocation nucleation problems, usually the length of band beyond the saddle point is much longer than that before the saddle point, so by the FENEB, we can reduce the overall number of replicas used while maintaining a relatively higher density of replicas around the saddle point, thus significantly increasing the efficiency and accuracy. In the present study, we use eight replicas for each individual calculation. The energies of the final configurations are at least 0.1 eV lower than those of the initial configurations. The specimen with a one-Burgers-vector height step was relaxed at 300 K for 100 ps and then cooled down to low temperature for FENEB calculation. The Quickmin algorithm (26), which is a damped dynamics method for minimizing a system's energy, was used to update atomic positions during FENEB calculation. The FENEB calculations were considered to be converged when the force on each replica is below 0.001 eV/Å or the calculation step exceeds a significant large number (100,000 steps) such that the activation energy rarely changes with even more calculation steps.

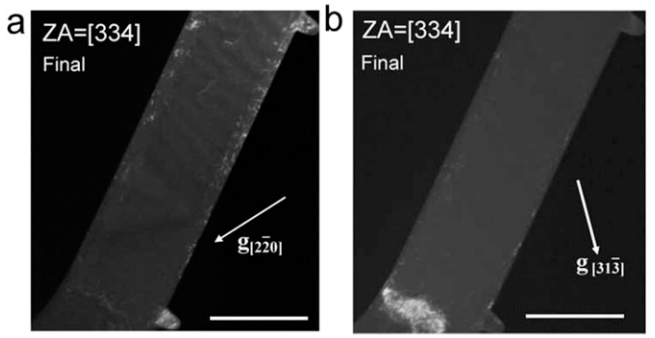

Fig. S1. Dark-field TEM images of the Al sample shown in Fig. 1 after mechanical healing in the main text. (*A*) $\boldsymbol{g} = [2\bar{2}0]$; (*B*) $\boldsymbol{g} = [31\bar{3}]$. (Scale bars, 500 nm.) Bold text ***g*** denotes a reflection vector.

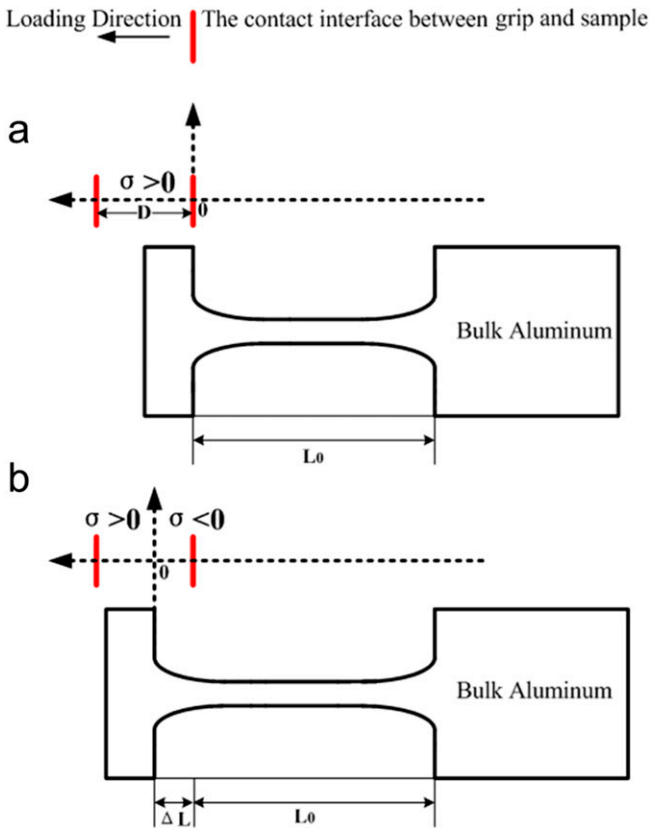

Fig. S2. Schematic illustration of the origin of the compressive stress upon unloading. (*A*) Programmed specimen setup. (*B*) Once plastic deformation sets in, the zero stress position would be shifted by a distance that is equal to the plastic elongation of the sample (Δ*L*).

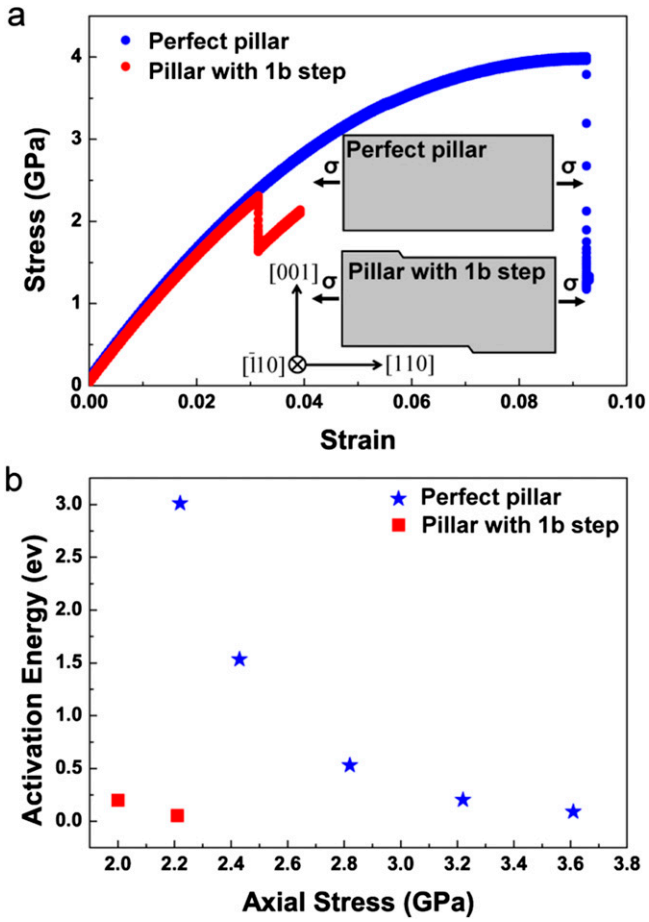

Fig. S3. Atomistic simulations of the mechanical behavior of pristine aluminum pillars without and with a surface step. (*A*) Strain–stress curves (from quasistatic athermal loading) for a perfect pillar and a pillar with a 1*b* step. *Inset* shows the simulation setup for these two cases. (*B*) Activation energy as a function of axial stress computed using the free-end nudged elastic band (FENEB) method.

Table S1. Visibility of dislocations with various Burgers vectors (2*b*) under different reflection vectors (*g*) in the TEM

	2***b***					
	$\pm[110]$	$\pm[1\bar{1}0]$	$\pm[101]$	$\pm[10\bar{1}]$	$\pm[011]$	$\pm[01\bar{1}]$
$\boldsymbol{g} = [1\bar{1}1]$	×	√	√	×	×	×
$\boldsymbol{g} = [2\bar{2}0]$	×	√	√	√	√	√
$\boldsymbol{g} = [31\bar{3}]$	√	√	×	√	√	√

The symbols "√" and "×" denote visible and invisible, respectively. Bold text indicates a vector.

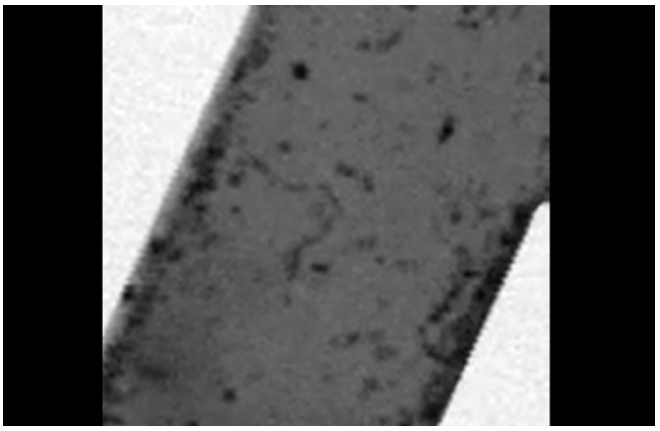

Movie S1. In situ TEM observation of oligodynamic motion of dislocation and abrupt depinning in response to the low-amplitude cyclic loading.

Movie S1

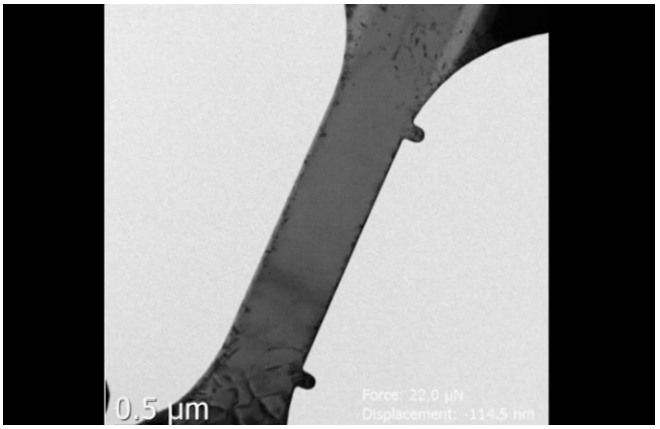

Movie S2. In situ TEM observation of dislocation nucleation near the markers due to stress concentration.

Movie S2